Graphene Anti-Dot Terahertz Plasmonic Metasurfaces Employing Self-Aligned Metal Cores for Sensing Applications

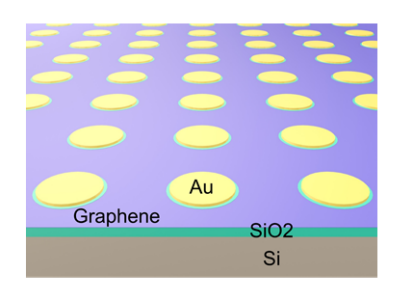
Xianglong Miao, Geng Li, Licheng Xiao, Peter Q. Liu*

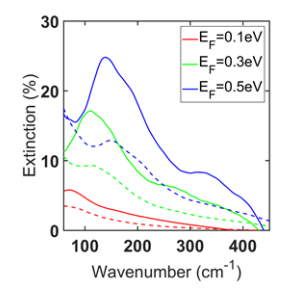
Department of Electrical Engineering, University at Buffalo, The State University of New York, Buffalo, New York 14260, United States

Abstract: Surface plasmons in graphene have great potential for molecular sensing applications thanks to their exceedingly high sensitivity to environmental changes. Here, we demonstrate a type of hybrid graphene-metal metasurface which supports strong graphene plasmonic resonances in terahertz range. Each unit cell of such a hybrid metasurface consists of a graphene anti-dot enclosing a metal disk realized using a self-aligned photolithography process. This hybrid design combines the advantages of both graphene and metal based photonic structures, leading to ~3 times stronger tunable plasmonic resonances and an order of magnitude larger near-field intensity enhancement with respect to those of bare graphene anti-dot metasurfaces.

Keywords: graphene; terahertz; plasmonics; metasurface, nanophotonics, sensing.

TOC Graphic





Text

Thanks to its various advantageous optical and electrical properties, graphene has recently been employed to develop a variety of nanophotonic devices such as modulators¹⁻⁴, photodetectors⁵⁻ 7, sensors⁸⁻¹² and light sources¹³. In particular, graphene supports surface plasmons with highly tunable optical responses in the mid-infrared to terahertz (THz) range¹⁴⁻¹⁷. Moreover, graphene surface plasmons (GSPs) feature deep subwavelength field confinement and thus extremely strong near-field enhancement and light-matter interactions¹⁸, which offer great opportunities in sensing and nonlinear optics areas 19-20. As monolayer graphene produced by chemical vapor deposition (CVD) becomes widely available, a variety of tunable plasmonic structures based on patterned graphene have been demonstrated and extensively studied, including arrays of graphene ribbons^{8-10,14-15}, disks^{11,16} and anti-dots²¹⁻²⁵. These graphene plasmonic structures, which are essentially highly tunable metasurfaces, form a suitable platform for surface enhanced infrared absorption (SEIRA) spectroscopy, and have been demonstrated to have great potential for quantitative protein detection and molecule identification 9-10,26-27. However, partly due to the limited carrier density tuning range and mobility of CVD graphene, the resonant optical responses of the experimentally demonstrated graphene plasmonic structures are not as strong as those of metasurfaces consisting of typical metallic resonators. For example, the transmission extinction at the resonance of various monolayer graphene plasmonic structures is usually below 10%8-11,14-15. This is especially the case for graphene anti-dot arrays which exhibit a transmission extinction of below 3%²²⁻²⁴. Therefore, effective approaches to enhancing the optical responses of graphene plasmonic structures need to be developed, so that the capability of GSPs for mediating strong light-matter interactions can be utilized in a broader

range of applications. One of the effective approaches is to employ hybrid metal-graphene nanophotonic structures³⁻⁴. Incident light can couple strongly to metallic antennas and be confined to subwavelength length-scale, which will in turn excite GSPs in graphene structures more efficiently. Recently, a variety of hybrid graphene-metal structures with strong and tunable optical responses have been demonstrated^{3-4,26-29}.

Here, we experimentally demonstrate a type of hybrid graphene-metal metasurface which employs gold disks inserted in graphene anti-dots to drastically enhance the strengths of the tunable graphene plasmonic resonances in the THz range. The resonant transmission extinction of such hybrid metasurfaces is enhanced by ~3 times compared to that of bare graphene anti-dot metasurfaces. In addition, our simulation shows that the metallic core leads to an order of magnitude enhancement of the near-field intensity of the resonant graphene plasmonic modes. Another advantage of our hybrid structure designs is that the minimum feature size of ~100 nm is conveniently realized with a self-aligned photolithography-based fabrication process which has minimal complexity increase compared to fabricating bare graphene anti-dot arrays.

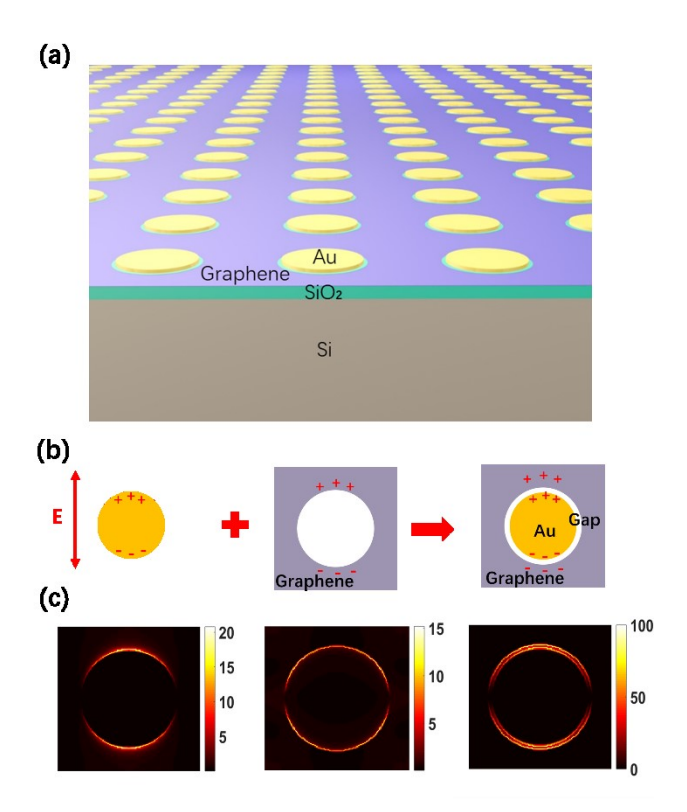


Figure 1. (a) Schematic of hybrid structure. (b) Illustration of the design rationale of the hybrid structures. (c) Near-field intensity distribution corresponding to the structures in (b): from the left to right are gold disk, graphene anti-dot, and hybrid structure, respectively.

Figure 1(a) shows the schematic of our hybrid structure design, which is based on graphene anti-dot array plasmonic metasurface²²⁻²³. A thin gold disk is inserted in each graphene anti-dot unit cell with a small (~100 nm) gap between their edges. The gold disk essentially functions as a THz optical antenna which can significantly concentrate the electric field (and energy) of an incident THz wave near the thin edges of the gold disk in sub-wavelength scale (see Figures 1(b)-(c)) and in a broad frequency range. This is also known as the lightning-rod effect³⁰⁻³¹. Such enhanced near fields near the gold disk edges in turn lead to more efficient excitation of graphene anti-dot plasmonic resonances, and hence improving the overall optical response of the hybrid structures. An important advantage of this design strategy is that the field enhancement due to the lightning rod effect occurs in a broad spectral range, and therefore

is not limited by the resonance frequency of the metallic optical antenna or the plasma frequency of the metal (see Supporting Information S1). It can be seen from Figure 1(c) that the hybrid structure indeed exhibits a significantly larger near-field enhancement compared to the bare graphene anti-dot or the gold disk alone. As discussed below, the gap size is one of the critical parameters determining the performance of these hybrid structures. We use Si/SiO₂ substrate for these hybrid metasurfaces in which the doped Si functions as a back-gate for tuning graphene carrier density.

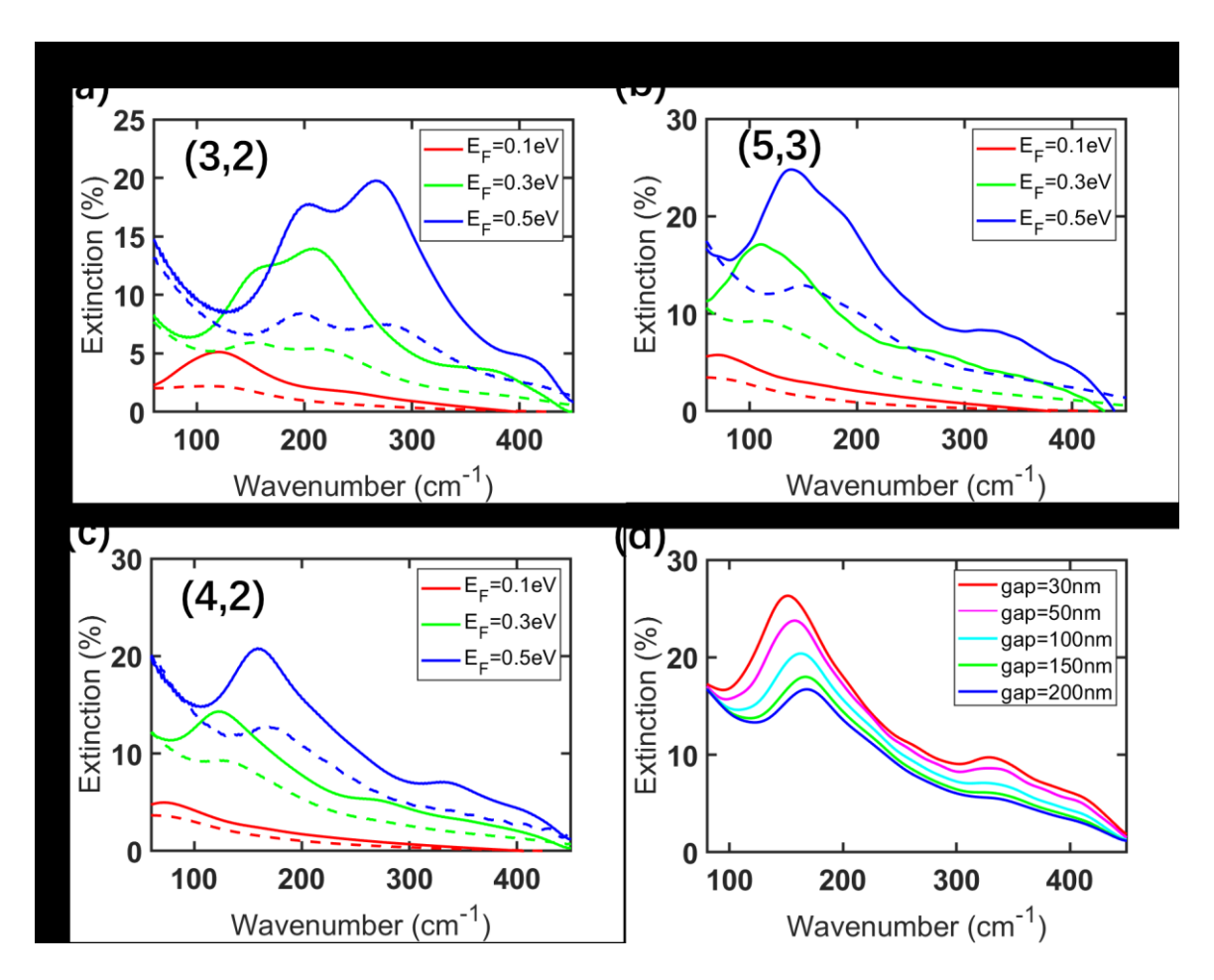


Figure 2. Simulated transmission extinction spectra of various hybrid anti-dot structures in comparison with those of the corresponding bare anti-dot structures. (a) The structures with index (3, 2). (b) The structures with index (4, 2). (c) The structures with index (5, 3). Solid lines are for the hybrid anti-dot structures and dashed lines are for the bare anti-dot structures. (d) Simulated transmission extinction spectra of the hybrid structure (4, 2) with various gap sizes. The Fermi level of graphene is set to 0.5 eV and the carrier scattering rate is 5 meV.

We design and optimize the performance of such hybrid metasurfaces using a simulation tool based on finite difference time domain method (see Supporting Information S2). Figures 2(a)-(c) show the transmission extinction spectra of 3 examples, in which the index (p, d) represents the periodicity p and the diameter d, respectively, of the graphene anti-dots arranged in squarelattice configuration. The gap between the gold disk edge and the graphene edge is set to be 100 nm, which is an optimized parameter (as discussed later). In each figure, the transmission extinction spectra of each hybrid structure at various Fermi levels are compared with those of the bare graphene anti-dot array with the same geometric parameters (i.e. periodicity and diameter). All structures exhibit clear GSP resonances at different frequencies in the THz range; however, the common feature of all the designed hybrid structures is that the transmission extinction due to the GSP resonances is enhanced by 2 to 3 times compared to that of the corresponding bare graphene anti-dot arrays. There is also a small red-shift of the GSP resonance peaks for the hybrid structures, which can be attributed to the reduction of the restoring force for the GSP oscillation as a result of image charges forming in the gold disks (i.e. screening of the GSPs by the gold disks). The THz resonance peaks of all the structures exhibit significant frequency tuning by about 100 cm⁻¹ (3 THz) as the Fermi level varies from 0.1 eV to 0.5 eV. The frequency tuning follows the scaling law $\omega \propto n^{\frac{1}{4}} \propto \sqrt{E_F}$ which is a unique characteristic of GSPs¹⁴.

The gap size between the graphene edge and the gold disk edge is a critical factor determining the device performance, and therefore we conduct systematic simulation to determine its optimal value. Figure 2(d) shows the transmission extinction spectra of a hybrid structure design assuming various gap sizes. For larger gaps, the enhancement of the GSP resonances

due to the field concentration of gold disks is less significant, whereas for smaller gap sizes, the gold disks cause more significant screening (frequency redshift) of the GSP resonances. It also becomes challenging for reliable device fabrication if the designed gap size is too small (below 50 nm). Considering these trade-offs, we determine the optimal gap size to be in the range of 50 to 100 nm for our experimental demonstration of such hybrid metasurface designs, which can readily achieve one order of magnitude enhancement of the field intensity (see Supporting Information S3).

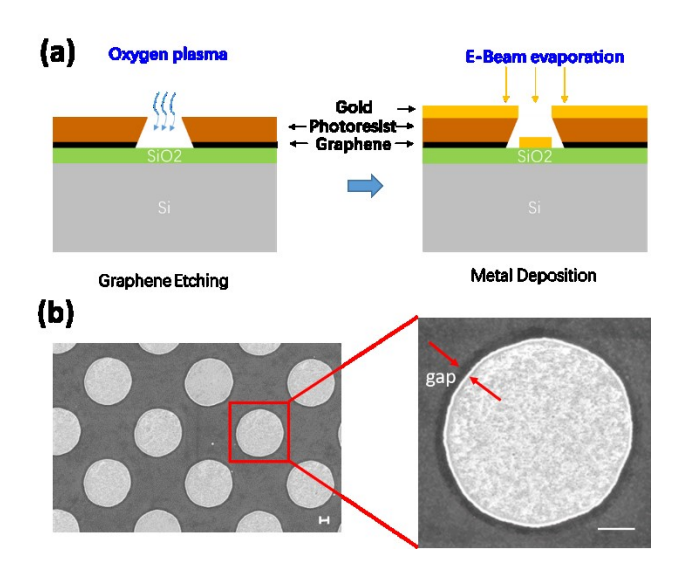


Figure 3. (a) Schematic of the key steps of the device fabrication process for realizing self-aligned gold disks in graphene anti-dots. (b) SEM images of a fabricated device. The right figure is a zoom-in part of the left one. The gap size varies within \sim 70 to 120 nm. The scale bars in the image correspond to 500 nm.

Due to the small gap size, it would be challenging to reliably fabricate a large-area (millimeter scale and above) metasurface employing such hybrid unit cell using a two-step electron beam lithography process. Therefore, we develop instead a one-step self-aligned photolithography-based process which proves to be capable of realizing the small gaps with satisfying accuracy across a large area, without introducing significant fabrication complexity compared to fabricating bare graphene anti-dot arrays. As illustrated in Figure 3(a), anti-dots of a reversible

photoresist (AZ5214E) are first patterned on the graphene using photolithography so that an undercut profile of photoresist sidewall is formed. After etching graphene with oxygen plasma to form graphene anti-dots, Ti/Au (5 nm/50 nm) is deposited on the sample surface using an electron-beam evaporator, and hence self-aligned gold disks are formed in the graphene antidots. The undercut profile of the photoresist sidewall leads to a small gap between the edge of the gold disks and the edge of the graphene anti-dots. Since the undercut profile of the photoresist depends on parameters including the thickness of photoresist and the exposure dose, we can control the gap size to some extent by fine tuning these relevant process parameters. Figure 3(b) shows an SEM image of a small region of a fabricated device, in which the patterned graphene and the periodic gold disks are clearly seen. In the zoomed image in Figure 3(b), the gap is observed to vary typically in the range of \sim 70 to 100 nm, and can be as large as ~120 nm at some locations. According to the simulation results in Figure 2(d), such a gap size variation is expected to cause inhomogeneous resonance broadening and lower resonance enhancement factors. Nevertheless, significant enhancement of the GSP resonances should be achieved with such a gap size variation range.

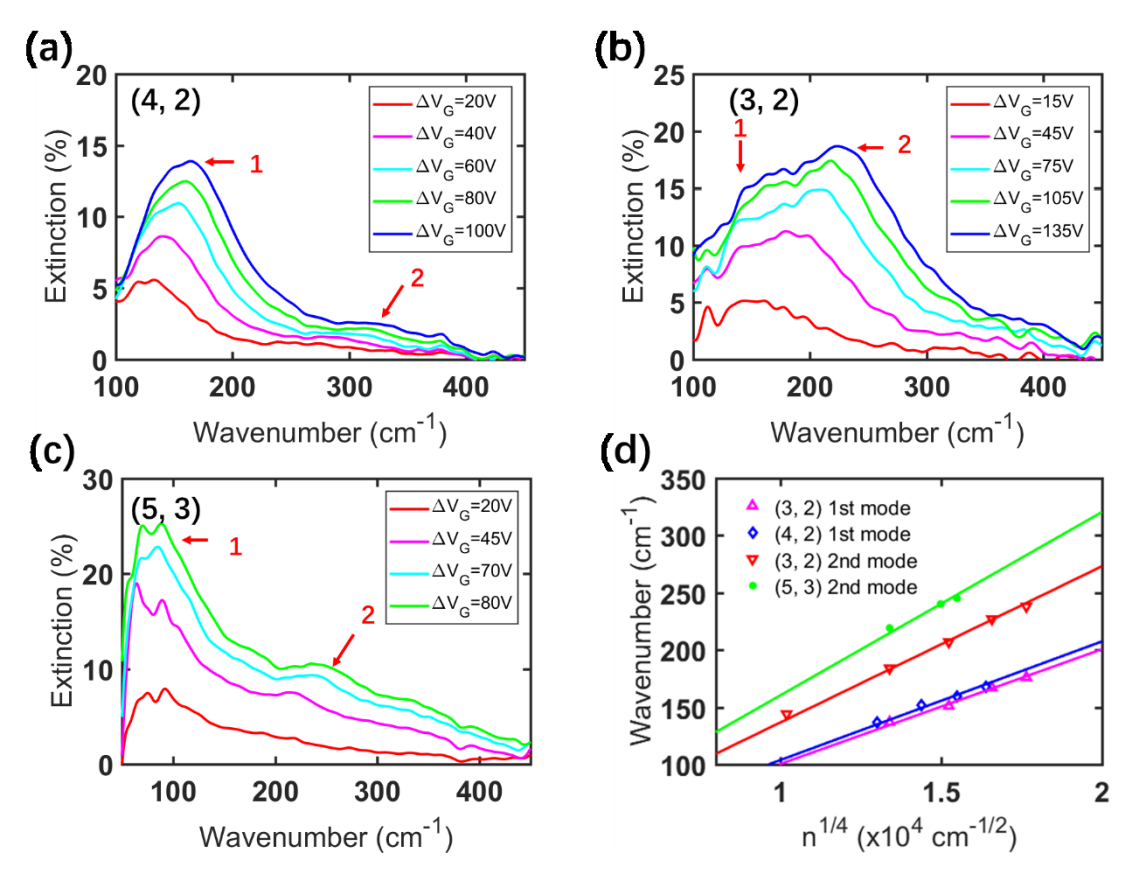


Figure 4. (a)-(c) Experimentally measured transmission extinction spectra of different devices of the specified geometries. The red arrows indicate different resonant modes of each device. (d) Extracted frequencies of the resonant GSP modes of different devices versus the graphene carrier density n (plotted as $n^{1/4}$). The symbols are the extracted experimental values. The solid lines are fitting results of the experimental data using the formula $\omega = A \cdot n^{1/4}$, where A is a fitting parameter.

We fabricate several hybrid graphene-metal metasurfaces and characterize their transmission extinction spectra at various graphene carrier densities (back gate voltages) using a Fourier transform infrared spectrometer (see Supporting Information S4). Figure 4 shows the measured transmission extinction spectra of several fabricated devices of the specified geometries. Similar to the simulation results, different resonant modes can be observed in the measured transmission extinction spectra of different hybrid structures. The discrepancies between the measured and the simulated spectra are mainly due to fabrication variation which lead to sample geometries being different from the designs. The transmission extinction peaks of these

hybrid devices are clearly a few times stronger than those of the corresponding graphene antidot devices reported in Ref. 23. Although the main resonance peak of the hybrid device (5, 3) is difficult to accurately identify due to the limited frequency range of our measurement system, its transmission extinction reaches as high as 25%, which is ~4 times that of the bare anti-dot (5, 3) device. It is also interesting to notice that thanks to the enhancement induced by the gold disks, some higher-order GSP resonance modes of the hybrid devices are clearly observed (e.g. the 2nd resonance mode of the (4, 2) and (5, 3) devices), whereas the corresponding modes are not as visible in the spectra of the bare graphene anti-dot structures. All the observed GSP resonance peaks shift to higher frequency when the gate voltage is tuned from 15 V to 135 V (corresponding to graphene Fermi level varying from ~0.14 eV to ~0.41 eV). All the extracted resonance frequencies follow the carrier density-dependent frequency scaling law of GSPs $(\omega \propto n^{\frac{1}{4}} \propto \sqrt{E_F})$ as shown by the fitting results in Figure 4(d).

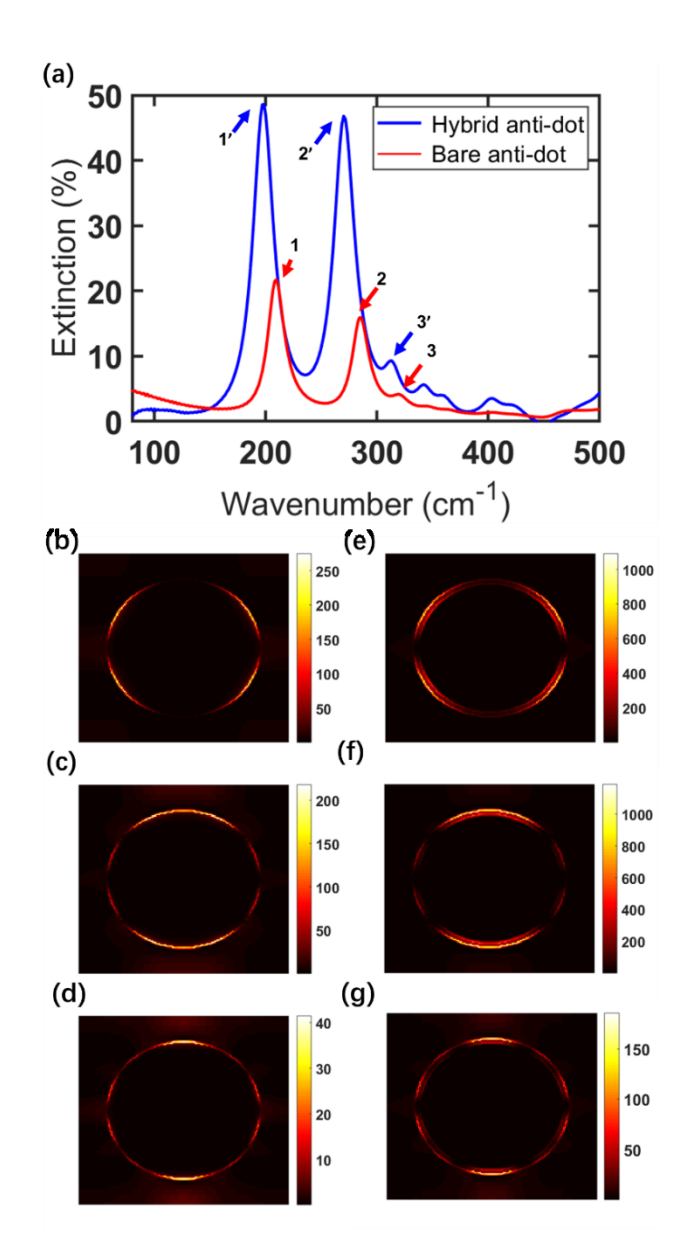


Figure 5. (a) Transmission extinction spectrum of the hybrid anti-dot metasurface (3, 2) in comparison with that of the bare graphene anti-dot metasurface (3, 2), assuming a carrier scattering rate of 1 meV. The different modes are labeled by the numbers 1–3 and 1'–3'. (b)-(d) Electric field intensity distributions of the modes 1–3 of the bare graphene anti-dot metasurface in (a), respectively. (e)-(g) Electric field intensity distributions of the modes 1'–3' of the hybrid anti-dot metasurface in (a), respectively.

To better understand the observation that some higher-order modes are clearly visible only in the spectra of the hybrid structures, we further simulate the hybrid structures assuming a lower carrier scattering rate (corresponding to 1 meV in energy), in order to obtain sharper resonance peaks which makes it easier to analyze their relative enhancement due to the gold disks. In the

simulated transmission extinction spectra shown in Figure 5 (and in Figure S8 of the Supporting Information), sharp resonance peaks of different modes are clearly observed. The enhancement of transmission extinction at the resonance peaks of the hybrid structure with respect to those of the bare graphene anti-dot structure are different for the three modes marked in Figure 5(a), which are calculated to be 2.2, 2.9 and 2.3, respectively. Since the enhancement (for both transmission extinction and near-field intensity) is partially determined by the overlap between the field profile of the gold disk (see Figure 1(c)) and those of the resonant GSP modes of the graphene anti-dots (Figures 5(b)-(d)), the second resonant mode in Figure 5(a) exhibits a larger enhancement factor as a result of its field profile matching that of the gold disk better. Despite the large field intensity enhancement, the near-field profiles of all the resonant GSP modes are not significantly altered by the presence of the gold disks, as can be seen from Figures 5(e)-(g) in comparison with Figures 5(b)-(d). It is also interesting to note that the transmission extinction of even higher order resonant GSP modes of some graphene anti-dot geometries can be enhanced by even larger factors (see Supporting Information S5). Due to the higher spatial confinement, these even higher order GSP modes couple weakly with incident plane waves. However, the highly confined and enhanced near-fields of the gold disks can excite these higher order GSP modes more effectively and efficiently, and hence the enhancement factors can be more significant.

In summary, we demonstrate a type of hybrid graphene-metal metasurface employing graphene anti-dots enclosing self-aligned gold disk cores. The gold disks function as THz optical antennas which effectively enhance the interaction between incident light and the tunable GSP resonances of the graphene anti-dots. Compared to the bare graphene anti-dot structures, the

hybrid structures show ~3 times stronger optical response (e.g. transmission extinction) and

about an order of magnitude higher near-field intensity at the GSP resonances. These simple

hybrid structure designs allow us to employ a self-aligned photolithography fabrication

process, which reliably achieves ~100 nm critical feature size across large device areas. This

hybrid graphene-metal metasurface design strategy and the convenient self-aligned fabrication

process can be applied to other types of graphene-based plasmonic structures to further enhance

various light-matter interactions for a broad range of applications, such as photodetectors,

sensing and nonlinear optics.

ASSOCIATED CONTENT

Supporting Information Available: Optical Response of Gold Disk; Numerical Simulation

Method; Gap Size Dependence of Near Field Enhancement; Device Fabrication and

Characterization; Enhancement of Different GSP Modes.

The Supporting Information is available free of charge on the ACS Publications website at

http://pubs.acs.org.

AUTHOR INFORMATION

Corresponding Authors

*E-mail: pqliu@buffalo.edu.

NOTES

The authors declare no competing financial interest.

ACKNOWLEDGMENTS

This work was partially supported by the National Science Foundation under the award number ECCS-1847203.

REFERENCE

- 1. Lee, S. H.; Choi, M.; Kim, T. T.; Lee, S.; Liu, M.; Yin, X.; Choi, H. K.; Lee, S. S.; Choi, C. G.; Choi, S. Y.; Zhang, X.; Min, B. Switching Terahertz Waves with Gate-Controlled Active Graphene Metamaterials. *Nat. Mater.* **2012**, *11*, 936-941.
- 2. Sensale-Rodriguez, B.; Yan, R.; Kelly, M. M.; Fang, T.; Tahy, K.; Hwang, W. S.; Jena, D.; Liu, L.; Xing, H. G. Broadband Graphene Terahertz Modulators Enabled by Intraband Transitions. *Nat. Commun.* **2012**, *3*, 780.
- 3. Yao, Y.; Kats, M. A.; Shankar, R.; Song, Y.; Kong, J.; Loncar, M.; Capasso, F. Wide Wavelength Tuning of Optical Antennas on Graphene with Nanosecond Response Time. *Nano Lett.* **2014**, *14*, 214-219.
- 4. Liu, P. Q.; Luxmoore, I. J.; Mikhailov, S. A.; Savostianova, N. A.; Valmorra, F.; Faist, J.; Nash, G. R. Highly Tunable Hybrid Metamaterials Employing Split-Ring Resonators Strongly Coupled to Graphene Surface Plasmons. *Nat. Commun.* **2015**, *6*, 8969.
- 5. Xia, F.; Mueller, T.; Lin, Y. M.; Valdes-Garcia, A.; Avouris, P. Ultrafast Graphene Photodetector. *Nat. Nanotechnol.* **2009**, *4*, 839-843.
- 6. Gan, X. T.; Shiue, R. J.; Gao, Y. D.; Meric, I.; Heinz, T. F.; Shepard, K.; Hone, J.; Assefa, S.; Englund, D. Chip-Integrated Ultrafast Graphene Photodetector with High Responsivity. *Nat. Photonics* **2013**, *7*, 883-887.

- 7. Castilla, S.; Terres, B.; Autore, M.; Viti, L.; Li, J.; Nikitin, A. Y.; Vangelidis, I.; Watanabe, K.; Taniguchi, T.; Lidorikis, E.; Vitiello, M. S.; Hillenbrand, R.; Tielrooij, K.-J.; Koppens, F. H. L. Fast and Sensitive Terahertz Detection Using an Antenna-Integrated Graphene pn Junction. *Nano Lett.* **2019**, *19*, 2765-2773.
- 8. Li, Y.; Yan, H.; Farmer, D. B.; Meng, X.; Zhu, W.; Osgood, R. M.; Heinz, T. F.; Avouris, P. Graphene Plasmon Enhanced Vibrational Sensing of Surface-Adsorbed Layers.

 Nano Lett. 2014, 14, 1573-1577.
- 9. Rodrigo, D.; Limaj, O.; Davide Janner; Etezadi, D.; Abajo, F. J. G. d.; Pruneri, V.; Altug, H. Mid-Infrared Plasmonic Biosensing with Graphene. *Science* **2015**, *349*, 165-168.
- 10. Hu, H.; Yang, X.; Zhai, F.; Hu, D.; Liu, R.; Liu, K.; Sun, Z.; Dai, Q. Far-Field Nanoscale Infrared Spectroscopy of Vibrational Fingerprints of Molecules with Graphene Plasmons. *Nat. Commun.* **2016,** *7*, 12334.
- 11. Zundel, L.; Manjavacas, A. Spatially Resolved Optical Sensing Using Graphene Nanodisk Arrays. *ACS Photonics* **2017**, *4*, 1831-1838.
- 12. Zhu, Y.; Li, Z.; Hao, Z.; DiMarco, C.; Maturavongsadit, P.; Hao, Y.; Lu, M.; Stein, A.; Wang, Q.; Hone, J.; Yu, N.; Lin, Q. Optical Conductivity-Based Ultrasensitive Mid-Infrared Biosensing on a Hybrid Metasurface. *Light Sci Appl* **2018**, *7*, 67.
- 13. Kim Y. D.; Kim H.; Cho Y.; Ryoo J. H.; Park C. H.; Kim P.; Kim Y. S.; Lee S.; Li Y.; Park S. N.; Yoo Y. S. Bright Visible Light Emission from Graphene. *Nat. Nanotechnol.* **2015**, *10*, 676-681.

- 14. Ju, L.; Geng, B.; Horng, J.; Girit, C.; Martin, M.; Hao, Z.; Bechtel, H. A.; Liang, X.; Zettl, A.; Shen, Y. R.; Wang, F. Graphene Plasmonics for Tunable Terahertz Metamaterials. *Nat. Nanotechnol.* **2011**, *6*, 630-634.
- 15. Brar, V. W.; Jang, M. S.; Sherrott, M.; Lopez, J. J.; Atwater, H. A. Highly Confined Tunable Mid-Infrared Plasmonics in Graphene Nanoresonators. *Nano Lett.* **2013**, *13*, 2541-2547.
- 16. Yan, H.; Li, X.; Chandra, B.; Tulevski, G.; Wu, Y.; Freitag, M.; Zhu, W.; Avouris, P.; Xia, F. Tunable Infrared Plasmonic Devices Using Graphene/Insulator Stacks. *Nat. Nanotechnol.* **2012**, *7*, 330-334.
- 17. Yoon, H.; Forsythe, C.; Wang, L.; Tombros, N.; Watanabe, K.; Taniguchi, T.; Hone, J.; Kim, P.; Ham, D. Measurement of Collective Dynamical Mass of Dirac Fermions in Graphene. *Nat. Nanotechnol.* **2014**, *9*, 594-599.
- 18. Koppens, F. H.; Chang, D. E.; Garcia de Abajo, F. J. Graphene Plasmonics: a Platform for Strong light-Matter Interactions. *Nano Lett.* **2011**, *11*, 3370-3377.
- 19. Cox, J. D.; Marini, A.; Garcia de Abajo, F. J. Plasmon-Assisted High-Harmonic Generation in Graphene. *Nat. Commun.* **2017**, *8*, 14380.
- 20. Soavi, G.; Wang, G.; Rostami, H.; Purdie, D. G.; De Fazio, D.; Ma, T.; Luo, B.; Wang, J.; Ott, A. K.; Yoon, D.; Bourelle, S. A.; Muench, J. E.; Goykhman, I.; Dal Conte, S.; Celebrano, M.; Tomadin, A.; Polini, M.; Cerullo, G.; Ferrari, A. C. Broadband, Electrically Tunable Third-Harmonic Generation in Graphene. *Nat. Nanotechnol.* **2018**, *13*, 583-588.

- Zhu, X.; Wang, W.; Yan, W.; Larsen, M. B.; Boggild, P.; Pedersen, T. G.; Xiao, S.;
 J.; Mortensen, N. A. Plasmon-Phonon Coupling in Large-Area Graphene Dot and Antidot
 Arrays Fabricated by Nanosphere Lithography. *Nano Lett.* 2014, 14, 2907-2913.
- 22. Yeung, K. Y.; Chee, J.; Yoon, H.; Song, Y.; Kong, J.; Ham, D. Far-Infrared Graphene Plasmonic Crystals for Plasmonic Band Engineering. *Nano Lett* **2014**, *14*, 2479-2484.
- 23. Liu, P. Q.; Valmorra, F.; Maissen, C.; Faist, J. Electrically Tunable Graphene Anti-Dot Array Terahertz Plasmonic Crystals Exhibiting Multi-Band Resonances. *Optica* **2015**, *2*, 135-140.
- Gopalan, K. K.; Paulillo, B.; Mackenzie, D. M. A.; Rodrigo, D.; Bareza, N.; Whelan,
 P. R.; Shivayogimath, A.; Pruneri, V. Scalable and Tunable Periodic Graphene Nanohole
 Arrays for Mid-Infrared Plasmonics. *Nano Lett.* 2018, 18, 5913-5918.
- 25. Tamagnone, M.; Slipchenko, T. M.; Moldovan, C.; Liu. P. Q.; Centeno, A.; Hasani, H.; Zurutuza, A.; Ionescu, A. M.; Martin-Moreno, L.; Faist, J.; Mosig, J. R.; Kuzmenko, A. B.; Poumirol, J.-M. Magnetoplasmonic Enhancement of Faraday Rotation in Patterned Graphene Metasurfaces. *Phys. Rev. B* **2018**, *97*, 241410.
- Li, Z. Y.; Zhu, Y. B.; Hao, Y. F.; Gao, M.; Lu, M.; Stein, A.; Park, A. H. A.; Hone, J.
 C.; Lin, Q.; Yu, N. F. Hybrid Metasurface-Based Mid-Infrared Biosensor for Simultaneous
 Quantification and Identification of Monolayer Protein. ACS Photonics 2019, 6, 501-509.
- 27. Lee, I. H.; Yoo, D.; Avouris, P.; Low, T.; Oh, S. H. Graphene Acoustic Plasmon Resonator for Ultrasensitive Infrared Spectroscopy. *Nat. Nanotechnol.* **2019**, *14*, 313-319.

- 28. Gao, W.; Shu, J.; Reichel, K.; Nickel, D. V.; He, X.; Shi, G.; Vajtai, R.; Ajayan, P. M.; Kono, J.; Mittleman, D. M.; Xu, Q. High-Contrast Terahertz Wave Modulation by Gated Graphene Enhanced by Extraordinary Transmission through Ring Apertures. *Nano Lett.* **2014**, *14*, 1242-1248.
- 29. Alcaraz Iranzo, D.; Nanot, S.; Dias, E. J. C.; Epstein, I.; Peng, C.; Efetov, D. K.; Lundeberg, M. B.; Parret, R.; Osmond, J.; Hong, J. Y.; Kong, J.; Englund, D. R.; Peres, N. M. R.; Koppens, F. H. L. Probing the Ultimate Plasmon Confinement Limits with a van der Waals Heterostructure. *Science* **2018**, *360*, 291-295.
- 30. Liao, P. F.; Wokaun, A. Lightning Rod Effect in Surface Enhanced Raman Scattering. *J. Chem. Phys.* **1982**, *76*, 751-752.
- 31. Gersten, J. I. The Effect of Surface Roughness on Surface Enhanced Raman Scattering. *J. Chem. Phys.* **1980**, *72*, 5779-5780.